

Article

Historical aerial surveys map long-term changes of forest cover and structure in the central Congo Basin

Koen Hufkens^{1,2,*}, Thalès de Haulleville³, Elizabeth Kearsley¹, Kim Jacobsen^{1,3}, Hans Beeckman³, Piet Stoffelen⁴, Filip Vandelook⁴, Sofie Meeus⁴, Michael Amara⁵, Leen Van Hirtum⁵, Jan Van den Bulcke¹, Hans Verbeeck¹, Lisa Wingate²

¹ Ghent University, Ghent, Belgium;

² INRA, UMR ISPA, Villeneuve d'Ornon, France;

³ Royal Museum for Central Africa, Tervuren, Belgium;

⁴ Botanic Garden Meise, Meise, Belgium;

⁵ National Archives of Belgium, Brussels, Belgium;

* Correspondence: koen.hufkens@gmail.com

Version January 23, 2020 submitted to Remote Sens.



1 **Abstract:** Land Use and Land Cover change (LULCC) of African rainforest contribute to global carbon
2 emissions. Yet, most historical estimates of LULCC and their carbon emissions rely on non-spatially
3 explicitly data in the pre-satellite era (< 1972). Past studies have expanded this pre-satellite time
4 frame with declassified satellite surveillance data or aerial surveys, but none cover the Congo Basin.
5 Here, we use historical aerial survey photos to map the extent and structure of LULCC around
6 Yangambi, central Congo Basin, in 1958. Our study leveraged Structure-from-Motion to generate
7 a large orthomosaic covering 82800 ha, counting 733 million pixels, at a sub meter resolution and
8 geo-referenced to $\sim 4.7 \pm 4.3$ m. Primary forest in the orthomosaic was classified with a Convolutional
9 Neural Network Deep Learning approach. We used these data to quantify LULCC, landscape and
10 canopy complexity and scale above ground biomass between historical and contemporary condition.
11 We show a shift from historical highly structured industrial deforestation in 1958 (16200 ha), to
12 contemporary smallholder farming clearing (8800 ha), increasing landscape fragmentation and
13 forest edges. Efforts to quantify canopy texture and their link to carbon storage had limited to no
14 success. Our analysis provides an insight in key spatial and temporal patterns of deforestation and
15 reforestation at a multi-decadal scale and provide a historical context to land-cover and land-use
16 change spatial patterns for past and ongoing field research in the area.

17 **Keywords:** Aerial survey, data recovery, CNN, Deep Learning, SfM, Congo Basin

18 1. Introduction

19 Tropical ecosystem services are severely impacted by deforestation and forest degradation [1–3].
20 Not only does tropical forest Land-Use and Land-Cover Change (LULCC) constitute 10 to 15% of
21 the total global emissions [4], changes in forest fragmentation affect the forest structure and function.
22 Strong fragmentation effects decreases the number of large trees along forest edges [5,6], while species
23 composition and biodiversity are equally negatively affected [7–9]. Estimates show that 31% of carbon
24 emissions are caused by edge effects alone [10].

25 As such, anthropogenic factors through LULCC heavily affect forest structure and functioning
26 [10–12]. Accurate estimates of LULCC and forest canopy structure are therefore imperative to estimate
27 carbon emissions and other ecosystem services [1,2]. Remote sensing products have been key input as
28 they provide accurate spatial information to help estimate carbon emissions [1,13]. High resolution
29 aerial images provide scientists tools to monitor forest extent, structure and carbon emissions as canopy
30 texture is linked to above ground biomass [14–16]. Yet, these estimates are often limited in time to
31 recent decades [1,2,17,18].

32 Historical estimates of **Land-Use and Land-Cover (LULC)**, in the pre-satellite era (< 1972), exist
33 but generally rely on non-spatially explicit data (i.e socio-economic data) [2,17,19,20]. Efforts have
34 been made to use other geo-spatial data sources such as historical maps [21], declassified CORONA
35 satellite surveillance data across the US and central Brazil [22] as well as aerial surveys in post world
36 war II German [23]. Survey data across the African continent is less common, inaccessible or both.
37 Some studies do exist, as Buitenwerf *et al.* [24], Hudak and Wessman [25] and Okeke and Karnieli
38 [26] used aerial survey images to map vegetation changes in South African savannas and the Adulam
39 Nature Reserve, respectively, whilst Frankl *et al.* [27] and Nyssen *et al.* [28] mapped the Ethiopian
40 highlands of 1930's.

41 Despite the existence of large historical archives of aerial survey imagery for the central Congo
42 Basin (Figure 1, Appendix Figure 3) as of yet no studies have valorized these data. The lack of a
43 consistent valorization effort is unfortunate as the African rainforest is the second largest on Earth and
44 covers ~630 million ha, representing up to 66 Pg of carbon storage [29], and currently loses forest at an
45 increasing pace [30]. Given the impact of LULCC on the structure and functioning of central African
46 tropical forests, and their influence on both carbon dynamics [31] and biodiversity [9], accurate long
47 term reporting of historical forest cover warrants more attention [21].

48 Here, we use a combination of historical aerial photography and contemporary remote sensing
49 data to map long-term changes in the extent and structure of the tropical forest surrounding Yangambi,
50 in the central Congo Basin, effectively linking the start of the anthropocene [32] with current
51 assessments. Yangambi was, and remains, a focal center of forest and agricultural research and

52 development in the central Congo Basin. Past research in the region allows for thorough assessment of
53 land-use and land-cover change from a multi-disciplinary point of view, confronting us with complex
54 deforestation and land-use patterns.

55 We leverage Structure-from-Motion to generate a large orthomosaic of historical imagery and
56 develop a Convolutional Neural Network based forest cover mapping approach, based upon a
57 semi-supervised generated dataset extensively leveraging data augmentation. Our methodology
58 aims to provides a historical insight into important LULCC spatial patterns in Yangambi, such as
59 fragmentation and edge complexity. We further contextualize the influence of changes in the forest's life
60 history on past and current research into Above Ground Carbon (AGC) storage [31] and biodiversity
61 [9] in the central Congo Basin. Our fast scalable mapping approach for historical aerial survey data,
62 using limited supervised input, would further support long-term land-use and land-cover change
63 analysis across the central Congo Basin.

64 2. Methods

65 2.1. Historical data acquisition

66 Data for the central Congo Basin region, surrounding Kisangani, were collected in several flights
67 during the dry season of 1958 and 1959 (from 8/01/1958 to 20/02/1958 and from 28/12/1958 to
68 9/01/1959 respectively, see Appendix Figure 1) to generate topographic maps of the area, supervised
69 by the "Institut Géographique du Congo Belge" in Kinshasa (then Léopoldville). Black-and-White
70 infrared images (0.4 - 0.9 μm) were gathered along flight paths running mostly from west to east,
71 between **09:00 and 11:00** local time. Along a flight path continuous images were taken using a Wild
72 Heerburgg RC5a (currently Leica Geosystems) with an Aviogon lens assembly (114.83mm / f 5.6,
73 with a 90°view angle) resulting in square photo negative of 180 by 180 mm. Flights were flown at an
74 average absolute altitude of ~5200 m above sea level, covering roughly 18 530 km² at an approximate
75 scale of 1/40 000. The use of the integrated autograph system ensured timely acquisition of pictures
76 with a precise overlap (~1/3) between images. This large overlap between images together with flight
77 parameters would allow post-processing, using stereographs, to create accurate topographic maps.
78 Original data from this campaign are stored in the [Royal Museum for Central Africa](#) in Tervuren,
79 Belgium (Figure 1).

80 2.2. Site selection

81 We prioritised flight paths and images that contained current day permanent sampling plots,
82 larger protected areas, and past agricultural and forest research facilities (Figure 2). This selection
83 provides a comprehensive mapping of the Yangambi area and the life history of the forest surrounding

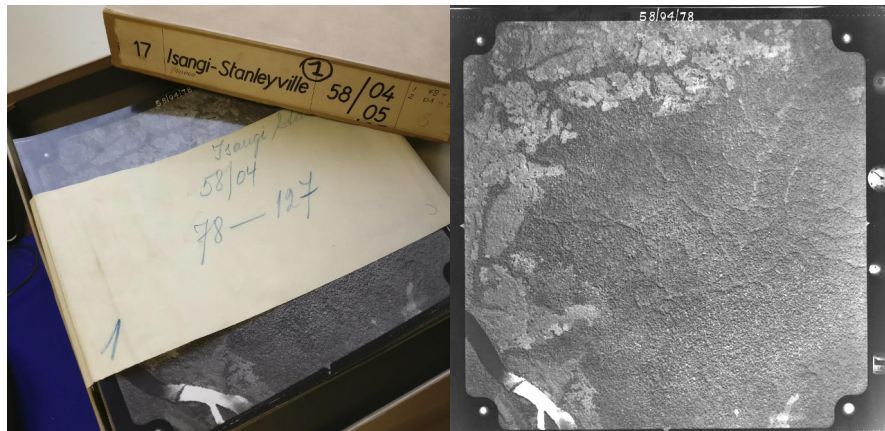


Figure 1. A box of historical aerial photographs (left) and a single aerial photograph (right) showing part of the Congo river. Note the meta-data provided in the margins of the image such as acquisition time and flight height and the solar glare on the Congo river.

84 it. Thereafter, we selected flight paths 1 through 11 for digitization. From this larger dataset of 334
 85 images we selected 74 survey images for orthomosaic compositing and further analysis. All the
 86 selected images stem from the flight campaign made during January and February of 1958. The area
 87 includes the Yangambi village, 20 contemporary permanent sampling plots [31], past and present
 88 agricultural experimental plots [33] and large sections of the Yangambi **UNESCO Man and Biosphere**
 89 **reserve** surrounding to the west and east of the village. Although not formally mosaicked we provided
 90 a full dataset of pre-processed images using the cropping and normalization routines described below.
 91 The latter data was not used in subsequent LULCC analysis, but has been archived and made available
 92 to the public separately (see code & data availability statement below).

93 2.3. Digitization and data processing

94 All selected images, covering the Yangambi area, were contact prints as original negatives of the
 95 prints were not available. Images were scanned at a resolution exceeding their original resolution
 96 (or grain) at the maximal physical resolution of an Epson A3 flatbed scanner (i.e. 2400 dpi or 160 MP
 97 per image) and saved as lossless tiff images. Data were normalized using contrast limited histogram
 98 equalization [34] with a window size of 32 and a clip limit of 1.5. Fiduciary marks were used to rectify
 99 and downsample the images into square 7700x7700 pixel images (~1200 dpi, 81 MP). This resulted in a
 100 dataset with digital images at a resolution that remained above the visible grain of the photographs,
 101 whilst the reduced image size facilitated easier file handling and processing speed.

102 Data was processed into a georeferenced orthomosaic using a Structure from motion (SfM, Ullman
 103 [35]) approach implemented in **Agisoft Metashape** version 1.5.2 (Agisoft LLC, St. Petersburg, Russia).
 104 An orthomosaic corrects remote sensing data to represent a perfectly downward looking image, free
 105 from perspective distortions due to topography and camera tilt. Using the SfM technique features,

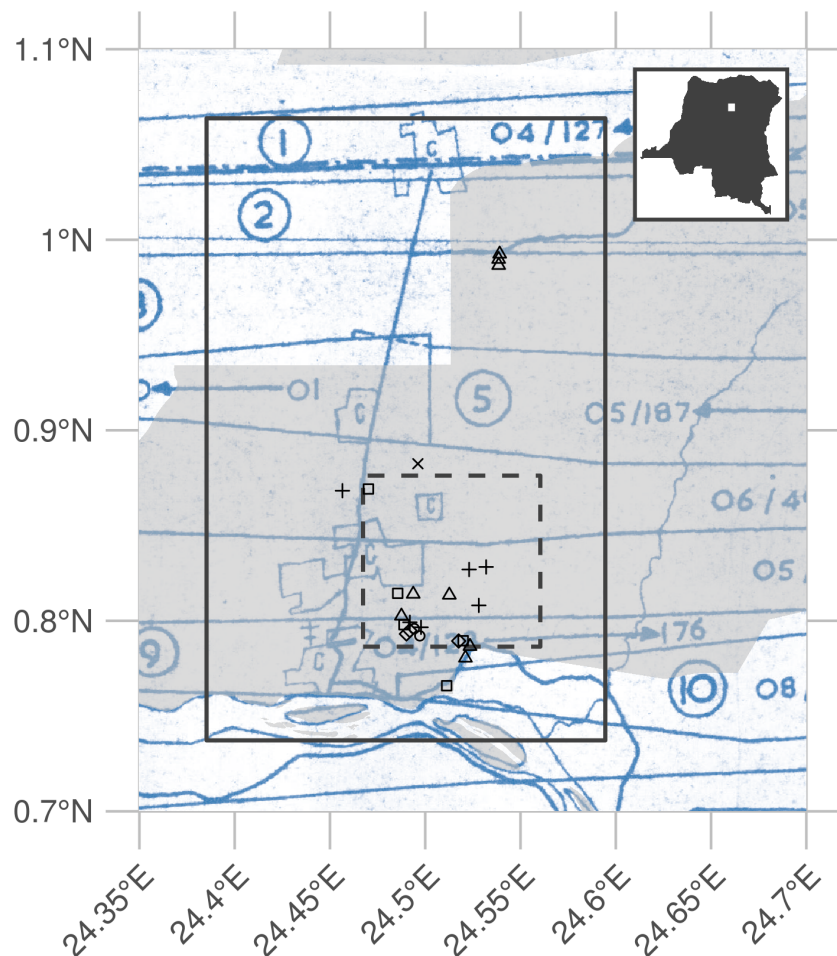


Figure 2. Overview of the historical flight paths during aerial photo acquisition and ancillary data used in this study. The bounding box of the orthomosaic data presented in this study is shown as a rectangle (23x36 km). The outline of a recent high-resolution Geo-eye panchromatic image is shown as a dashed dark grey rectangle (10x10km). The location of various permanent sampling plots are shown as x, +, and open squares and triangles for the mixed, mono-dominant and edge plots respectively. The grey polygon delineates the current day Yangambi Man and Biosphere reserve. The inset, top right, situates the greater Yangambi region (white rectangle) with the DR Congo. The full flight plan and details are shown in Appendix Figure 1 and 2

106 areas in images with a large degree of similarity, are matched across various images to reconstruct
107 a three dimensional scene (topography) from two-dimensional image sequences. During the SfM
108 analysis we masked clouds, glare or large water bodies such as the Congo river.

109 We calculated the orthomosaic using a low resolution point cloud and digital elevation map
110 (DEM). Additional ground control points were provided to assist in the referencing of image and
111 constrain the optimization routine used in the SfM algorithm. Ground control points consisted of
112 permanent structures which could be verified in both old and new aerial imagery (i.e. ESRI World
113 Imagery) and consisted of corner points of build structures (e.g. a building, bridge or swimming
114 pool etc.). Although clouds were removed during the SfM routine we did not mask all clouds in the
115 final orthomosaic to maximize forest coverage. The final scene was cropped, to provide consistent wall
116 to wall coverage of the reconstructed scene. The orthomosaic was exported as a geotiff for further
117 georeferencing in QGIS [36] using the georeferencer plugin (version 3.1.9) and additional ESRI World
118 Imagery high resolution reference data. We used 3rd degree polynomial and 16 ground control points
119 to correct the final image. Ground control points, raw image data and final processed image are
120 provided in addition to measures of uncertainty such as mean and median error across all ground
121 control points. All subsequent analysis are executed on the final geo-referenced orthomosaic or subsets
122 of it.

123 *2.4. Land-Use and Land-Cover Change*

124 *2.4.1. Classifying Land-Use and Land-Cover*

125 *Model training*

126 We automatically delineated all natural forest in the historical data, thus excluding tree plantations,
127 thinned or deteriorated forest stands which showed visible canopy cover loss, fields and buildings.
128 We used the Unet Convolutional Neural Net (CNN, Ronneberger *et al.* [37]) architecture implemented
129 in Keras [38] with an efficientnetb3 pre-processing backbone [39] running on TensorFlow [40] to train
130 a binary classifier (i.e. forest or non-forested). Training data were collected from the orthomosaic by
131 randomly selecting 513 pixel square tiles from locations within homogeneous forested or non-forested
132 polygons in the historical orthomosaic (Figure 5). Separate polygons were selected for training,
133 testing and validation purposes. Validation polygons were sampled 300 times, while both testing
134 and validation polygons were sampled at 100 random locations. Tiles extracted from locations
135 close to the polygon border at times contained mixed cover types. Tiles with mixed cover types
136 were removed from the list of source tiles (Table 1). Homogeneous source tiles were combined in
137 synthetic landscapes using a random gaussian field based binary mask (Figure 3). We generated 5000

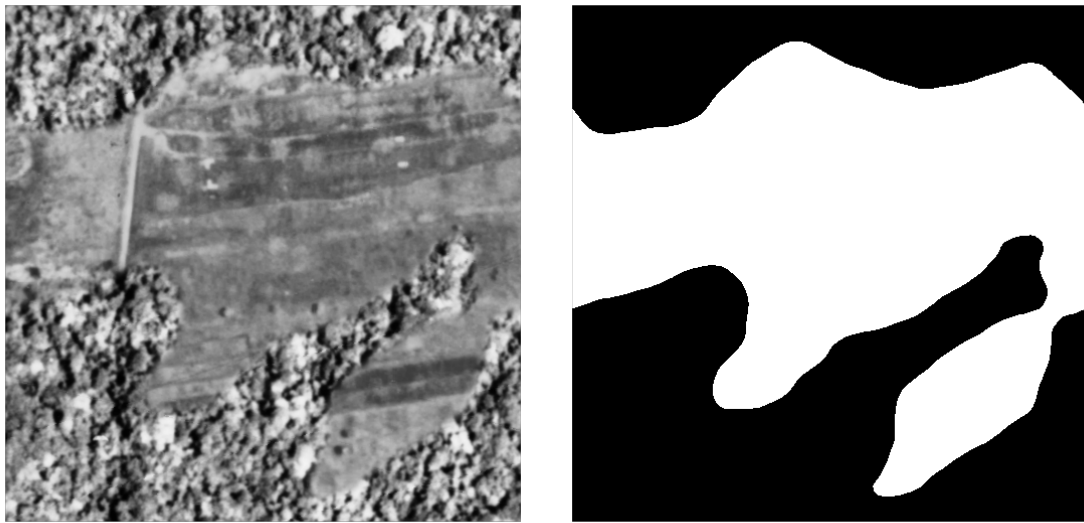


Figure 3. An example synthetic landscape, combining homogeneous forest and non-forest images into a patchy landscape using random gaussian field based masks. The left panel shows a combined synthetic landscape, while the right panel shows the corresponding forest (black) and non-forest (white) labels.

138 synthetic landscapes for training, while 500 landscapes were generated for both the validation and the
 139 testing datasets for a total of 6000 synthetic landscapes. In order to limit stitch line misclassifications,
 140 along the seams of mosaicked images, we created synthetic landscapes with different forest tiles
 141 to mimick forest texture transitions. We applied this technique to 10% of the generated synthetic
 142 landscapes (**across training, validation and testing data**).

Table 1. Number of source tiles used for the generation of synthetic landscapes.

	training	testing	validation
forest	300	100	100
non-forest	294	92	84

143 The CNN model was trained for 100 epochs with a batch size of 30 using Adam optimization [41],
 144 maximizing the Intersect-over-Union (IoU) using Sørensen–Dice and categorical cross-entropy loss
 145 functions. Data augmentation included random cropping to 320 pixel squares, random orientation,
 146 scaling, perspective, contrast and brightness shifts and image blurring. The optimized model was used
 147 to classify the complete orthomosaic using a moving window approach with a step size of 110 pixels
 148 and a majority vote (> 50% agreement) across overlapping areas to limit segmentation edge effects.
 149 **In addition we provide, raw pixel level classification agreement data for quality control purposes**
 150 **(see Data availability below)**. We refer to Figure 4 for a synoptic overview of the full deep learning
 151 learning workflow.

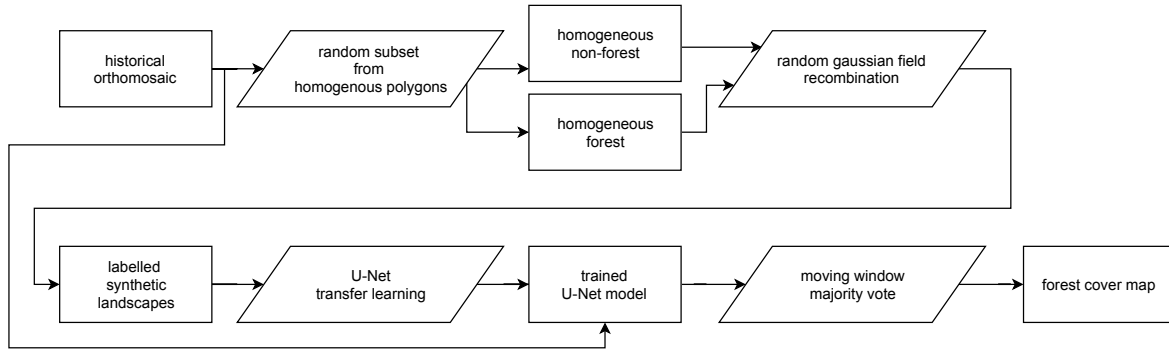


Figure 4. A diagram of the deep learning workflow followed in training a binary forest / non-forest cover convolutional neural net U-Net model to generate our forest cover map.

152 *Model validation*

153 We report the CNN accuracy based upon the IoU of our out-of-sample validation dataset
 154 of synthetic landscapes. In addition, we report confusion matrices for all pixels across the
 155 homogeneous validation polygons, as well as the training and testing polygons (see Figure
 156 5). Furthermore, we used the first acquisition of a recent pan-chromatic Geo-Eye 1 stereo pair
 157 (Geo-Eye, Thornton, Colorado, U.S.A., order 737537, 2011-11-11 08:55 GMT or 09:55 local time)
 158 to classify and assess the robustness of the CNN algorithm on contemporary remote sensing
 159 imagery with similar spectral and spatial characteristics. We used the Global Forest Change
 160 version 1.6 (GFC, tile 10N-020E) [1] map data, capturing forest loss up to 2011, to quantify accuracy
 161 on downsampled CNN Geo-Eye classification results. Once more, we report the confusion matrix
 162 of between the GFC and CNN derived forest cover maps, masking clouds and cloud shadows. To
 163 summarize confusion matrices we report accuracy as:

$$164 \quad Accuracy = \frac{(TP+TN)}{(TP+TN+FP+FN)}$$

165 in which TP, TN, FP, FN are True Positive, True Negative, False Positive and False Negative,
 166 respectively.

167 2.4.2. Characterizing long term change

168 To map long term land-use and land-cover change in the Yangambi region we used the
 169 contemporary Global Forest Change version 1.6 (GFC, tile 10N-020E) map data [1]. Using the GFC
 170 data we calculated the latest state of the forest with respect to the conditions at the start of 1958, 60
 171 years earlier. In our analysis we only included GFC pixels which recorded no **forest** loss throughout
 172 the whole 2000 - 2018 period. As the resolution of the historical forest classification exceeds that
 173 of the GFC map we downsampled our historical forest cover data to 30 m GFC resolution **using a**
 174 **nearest neighbour approach**. We masked out all water bodies using the Global Forest Change survey

175 data mask layer, and limited the analysis to the right bank of the Congo river. We provide summary
176 statistics of historical and contemporary forest loss and regrowth.
177 deforestation (persistent forest loss after 1958), reforestation (regrowth after loss in 1958).

178 2.4.3. Landscape fragmentation & Above Ground Carbon estimates

179 To quantify changes in the structure of forest cover and its disturbances we used spatial pattern
180 analysis landscape fragmentation metrics [42]. We report the ratio of edge to area and the fractal
181 index to quantify landscape complexity of forest disturbances. Statistics were calculated for all forest
182 disturbance patches larger than 1 ha and smaller than the 95th percentile of the patch size distribution
183 using the R package landscapemetrics [43]. We provide mean and standard deviation on edge, area,
184 their ratio and fractal dimension for both the historical and contemporary Hansen *et al.* [1] forest cover
185 maps.

186 We estimated above ground carbon (AGC) losses and gains over time using plot based averages
187 of recent inventory data at permanent sampling plots in the area (Figure 2). We refer to Kearsley *et al.*
188 [31] for the survey method and allometric relations used to scale the survey data. Unlike standard
189 square 1 ha plots edge plots were set back 200m from forest edges and were 50x200 m, with the 50
190 m side of the plot along the forest edge and continuing 200 m into the forest (Appendix Table 1). We
191 further confirmed that forest edge plots did not show a significantly different AGC compared to those
192 of non-edged / mixed forest plots (Mann Whitney U test, $p < 0.05$). Thus it was not necessary to
193 explicitly quantify changes in AGC caused by edge effects. Moreover, we used the mean values of the
194 mixed forest as representative for potential AGC losses. Despite the challenges inherent in quantifying
195 AGC for forest edges we mapped the total extent of the edges in the contemporary landscape. To
196 align our landscape analysis with exploratory analysis of the survey data we used a buffer of 200 m to
197 estimate the extent of forest edges and patches, up to the location of forest edge plots.

198 Surveys of old plantations show a large variation in AGC, depending on age and the crop type.
199 For example, the AGC values varied from 168.67 to 86.55 g Mg C ha⁻¹, for *Hevea brasiliensis* (rubber
200 tree) and *Elaeis guineensis* (oil palm) plots respectively (Bustillo *et al.* [44], personal communications).
201 These higher values are in line with the mixed AGC estimates in the area, while the palm plantations
202 resemble old-regrowth values (81.8 Mg C ha⁻¹, see **Appendix Table 1**). We therefore use both the
203 estimates of old-regrowth and mixed forest to estimate AGC for regrowth. We did not have sufficient
204 data to account for individual changes in AGC across plantations.

205 2.5. Canopy structure & FOTO texture analysis

206 We compared the structure of the canopy both visually and using Fourier Transform Textural
207 Ordination (FOTO, Couteron [45]). Fourier Transform Textural Ordination uses a principal component

208 analysis (PCA) on radially averaged 2D Fourier spectra to characterize canopy (image) texture. The
209 FOTO technique was first described by Couteron [45] to quantify canopy stucture in relation to biomass
210 and biodiversity, and can be used across multiple scenes using normalization [16].

211 We used the standard FOTO methodology with fixed zones, instead of the moving window
212 approach. The window size was set to the same size (187 pixels or ~150 m) as used in the moving
213 window analysis above. To account for illumination differences between the two scenes we applied
214 histogram matching. No global normalization was applied, as the scene was processed as a whole. PC
215 values from this analysis for all permanent sampling plots in both image scences were extracted using
216 a buffer with a radius of 50 m.

217 For both site based and scene analysis we correlate PC values with permanent sample plot
218 inventory data such as stem density, above ground biomass and tree species richness. Additional
219 comparisons are made between contemporary Geo-Eye data and the historical orthomosaic derived PC
220 values. Due to the few available permanent sampling plots in both scenes we used a non-parametric
221 paired signed rank (Wilcoxon) test to determine differences between the PC values of the Geo-Eye and
222 historical orthomosaic image scenes across mono-dominant and mixed forest types. In all analysis,
223 mono-dominant site 4 was removed from the analysis due to cloud contamination.

224 3. Results

225 3.1. Orthomosaic construction

226 Our analysis provides a first spatially explicity historical composite of aerial survey images **in**
227 **support of mapping land-use and land-cover** within the Congo Basin. The use of high resolution
228 historical images combined with structure from motion image processing techniques allowed us to
229 mosaic old imagery across a large extent. The final orthomosaic composition of the Yangambi region
230 **provided** an image scene covering approximately 733 million pixels across ~82800 ha (~23x36 km,
231 Figure 2). The overall accuracy of the SfM orthomosaic composition was 0.88 m/pixel using the sparse
232 cloud DEM for corrections at 45.8 m/pixel. The resulting georeferenced scene had a spatial accuracy
233 of approximately **23 m**. Further georeferencing outside the SfM workflow reduced the mean error at
234 the ground control points to 5.3 ± 4.9 px ($\sim 4.7 \pm 4.3$ m), with a median error of 2.9 px (2.6 m). The
235 orthomosaic served as input for all subsequent LULCC analysis with all derived maps provided with
236 the manuscript repository (see data & code availability statements below).

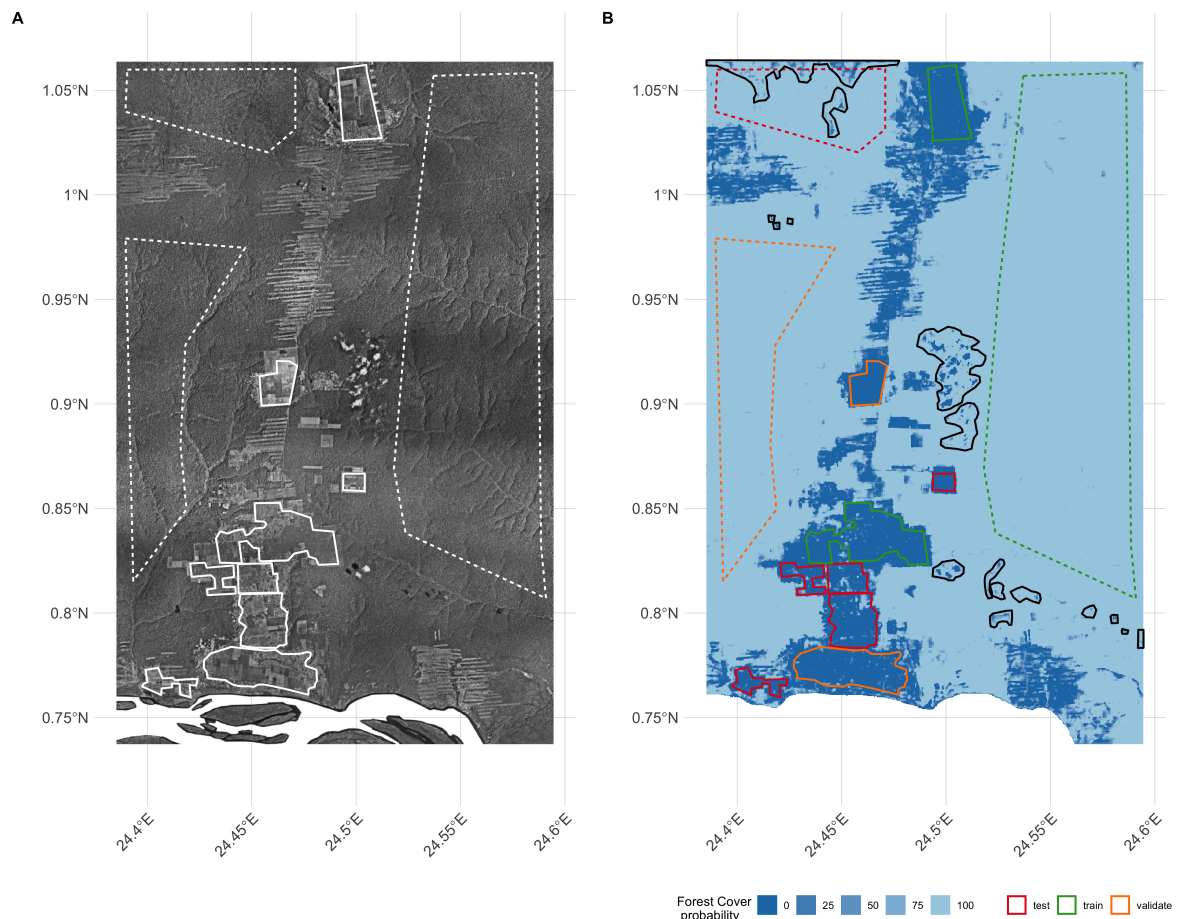


Figure 5. Overview of the final orthomosaic of the greater Yangambi region (A) as well as the forest cover classification uncertainty (B) used to generate the final Land Land Cover map (see Figure 6). Homogeneous polygons used in the generation of the synthetic landscape for Convolutional Neural Network training, testing and validation are marked as dashed and full lines for forest and non-forest regions, respectively. Training, testing and validation regions are denoted in panel B in green, red and orange, respectively. Black polygon outlines denote cloud and image stitch line regions which were manually excluded from analysis, but retained in calculation of validation statistics (see Table 2).

²³⁷ *3.2. Land-use and Land-Cover Classification*

²³⁸ *3.2.1. CNN model validation*

²³⁹ **The CNN deep learning classifier reached an Intersection-over-Union (IoU) accuracy of 97%**
²⁴⁰ **on the detection of disturbed forest in the out-of-sample (validation) synthetic landscape data.**
²⁴¹ **Using all pixels within the validation polygons (Figure 5) showed a similar accuracy value of**
²⁴² **~98%. Using all polygons across the scene, including those used in the generation of testing and**
²⁴³ **training synthetic landscapes, increased the accuracy to ~99% (Table 2). A comparison with recent**
²⁴⁴ **pan-chromatic Geo-Eye data shows good agreement, with an accuracy of ~87% across all pixels,**
²⁴⁵ **between the landsat based GFC data and downscaled CNN results (Table 2 and Figure 7).**

Table 2. Confusion matrix showing % agreement between forest / non-forest classes using a Convolutional Neural Network (CNN) across previously selected homogenous areas.

CNN	Geo-Eye (full scene)		Aerial Survey (all polygons)		Aerial Survey (validation polygons)	
	non-forest	forest	non-forest	forest	non-forest	forest
non-forest	10.17	8.55	97.4	0.19	98.59	0.0
forest	3.75	77.52	2.6	99.81	1.41	100.0
Accuracy	87.70		98.61		99.3	

²⁴⁶ *3.3. Long term LULC changes and Above Ground Carbon*

²⁴⁷ Scaling our classifier to the whole historical orthomosaic we detected **~16200 ha** (or ~20% of the
²⁴⁸ scene) of disturbed forests. A large fraction of the disturbed area was restored in the period between
²⁴⁹ the two **acquisition periods**. In total, **9918 ha**, or little over half of the affected forest was restored
²⁵⁰ (Figure 5C-D, dark blue). Recent deforested areas, as registered through satellite remote sensing,
²⁵¹ approximate **8776 ha** (Table 3, Figure 6 - light green).

²⁵² Recent deforestation follows a distinctly different pattern compared to historical patterns.
²⁵³ Historical deforestation showed a classical fishbone pattern for forest clearing with very sharp edges,
²⁵⁴ while current patterns are patchy and ad-hoc (figure 6C, dark blue and green colours respectively).
²⁵⁵ These differences are reflected in the analysis of landscape metrics of forest loss. Between the historical
²⁵⁶ and contemporary LULCC maps we see an increase in small disturbances, as indicated by the
²⁵⁷ decreasing area of the mean patch size, down to $\sim 1.86 \pm 0.75$ ha from $\sim 5.25 \pm 5.02$ ha historically.
²⁵⁸ Perimeter lengths were longer historically, at 1451 ± 943 m, compared to contemporary landscapes
²⁵⁹ $\sim 921 \pm 362$ m (Table 3). This shift in perimeter area ratio led to a similar change in the fractal index,
²⁶⁰ increasing in value to 1.1 ± 0.05 from 1.09 ± 0.04 over time. Values closer to a fractal index of 2 suggest
²⁶¹ a more complex (fragmented) landscape.

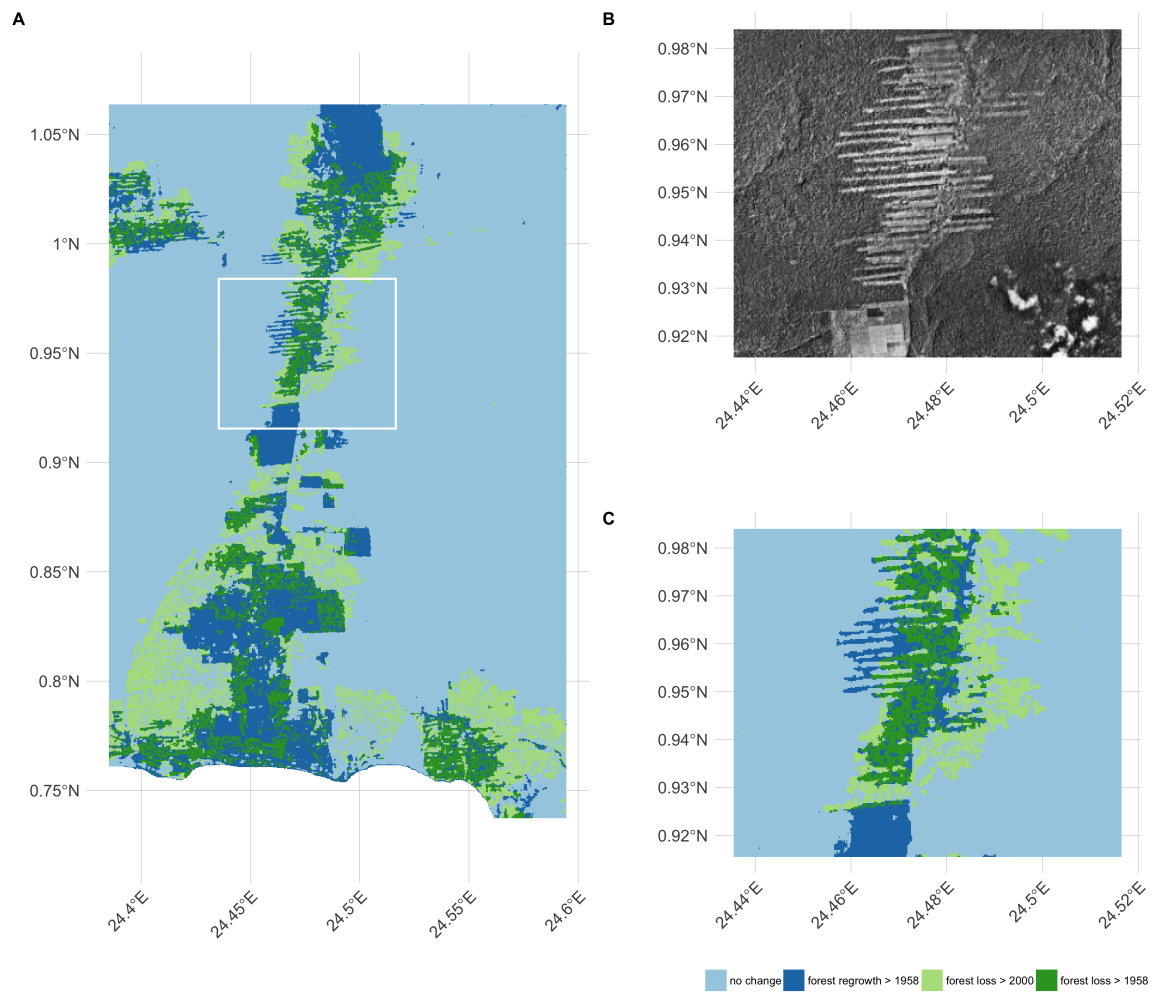


Figure 6. Overview of the final Land Use Land Cover Change map, a detailed inset of both the underlying orthomosaic (B) and the derived land use land cover change map displayed as the difference between the Convolutional Neural Network based classification orthomosaic and the recent Landsat based forest cover map by Hansen et al. 2013 (C).

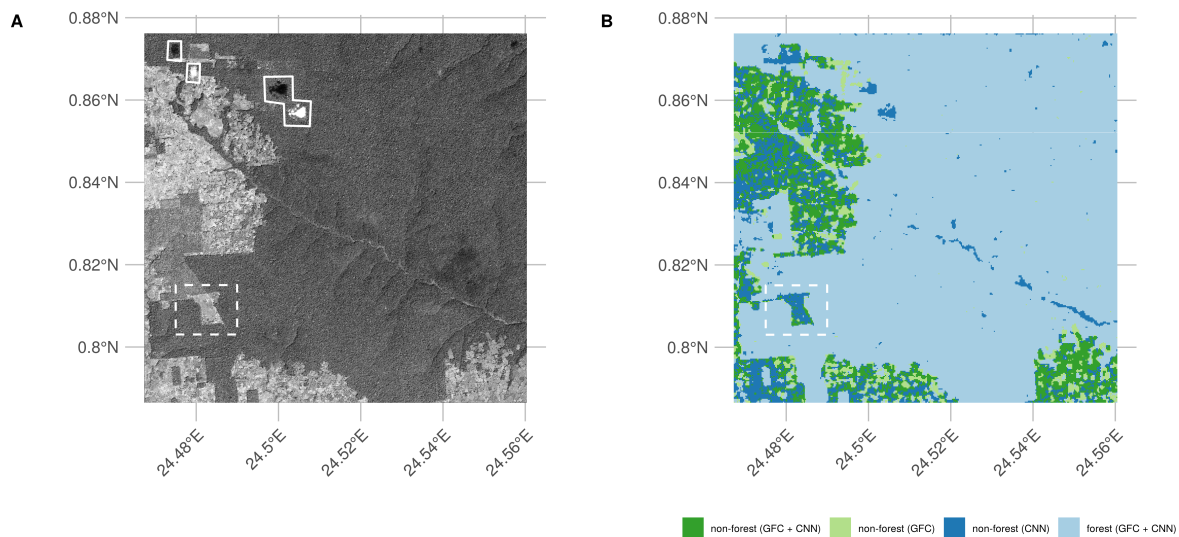


Figure 7. Convolutional Neural Network (CNN) based forest cover classification results (B) as run on a recent (2011) Geo-Eye panchromatic image (A). We show the difference between the Convolutional Neural Network based classification and a recent Landsat based forest cover map by Hansen et al. 2013. Full white outlines denote cloud contamination, the dashed rectangle shows a location where the CNN outperforms the Landsat based forest classification.

262 A comparison of forest edge plots with mixed forest plots showed no significant difference in
 263 AGC, or other reported values such as species richness, basal area or stem density (Mann Whitney U
 264 test, $p < 0.05$). Edge influence did not extend beyond 200 m from a forest edge, but still represented an
 265 area of **13151 ha**.

266 Changes in both land-use and land-cover led to concomitant changes in above ground carbon
 267 stocks. Recovery throughout the region was characterized for patches of forest and plantations.
 268 Assuming high density stands, based on previous work, this could amount to a carbon gains of 1592
 269 Gg C across our study area, offsetting more recent losses of approximately 1408 Gg C. On the other
 270 hand, at the low end, if we assume a lower carbon density of $81.8 \text{ Mg C ha}^{-1}$ this would result in a
 271 total carbon gain of 811 Gg C. Using our approach results indicate that overall deforestation around
 272 Yangambi has resulted in a loss of ~2416 Gg C in AGC stocks.

Table 3. Land use land cover change statistics of forest cover around Yangambi in the central Congo Basin. The data evaluates a difference between a historical (1958) aerial photography based survey and the Hansen et al. 2013 based satellite remote sensing data. Spatial coverage statistics are provided in square kilometers (km) and hectares (ha), rounded to the nearest integer as well as Above Ground Carbon (AGC) scaled using recent survey measurements.

	AGC	
	ha	(Gg C ha $^{-1}$)
Forest	68455	
- of which edges	13151	
Regrowth > 1958 loss	9918	811 - 1592
Loss > 2000	8776	1408
Loss > 1958 (permanent)	6282	1008

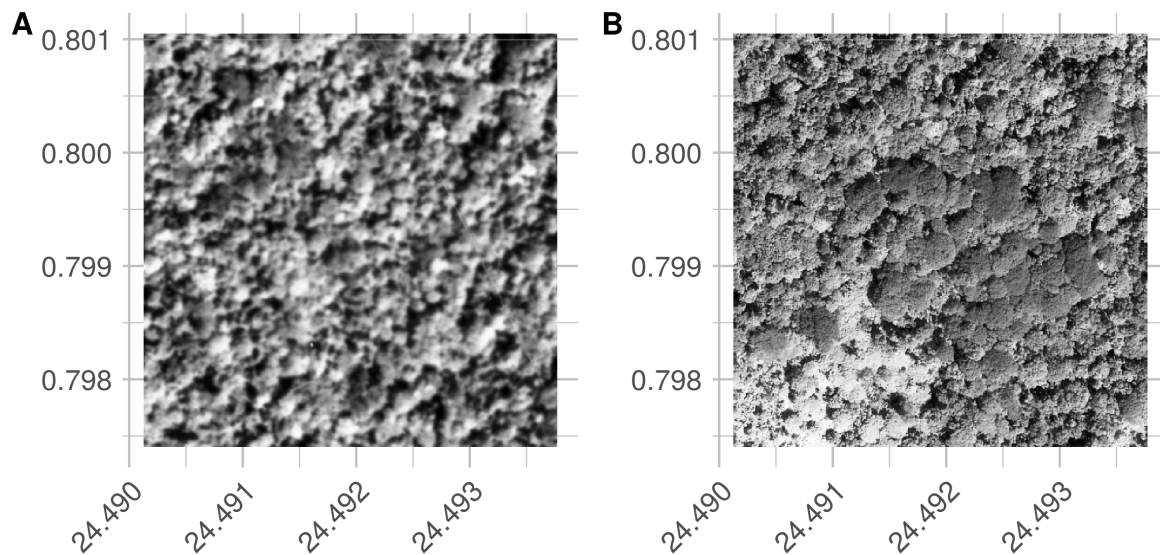


Figure 8. Visual comparison between a historical (A) and contemporary (B) permanent sampling plot. The site is currently listed as a mono-dominant *Brachystegia laurentii* stand. Note the structural differences with a 'coarser' canopy structure in the historical image compared to the more closed contemporary stand.

Table 4. Landscape metrics for historical and contemporary deforestation patterns. We report patch perimeter and area, their ratio and fractal dimension. Values are reported as mean \pm standard deviation, across all deforestation patches.

	perimeter (m)	area (ha)	ratio (m^{-1})	fractal dimension
historical	1451.58 ± 943.27	5.25 ± 5.02	0.03 ± 0.01	1.09 ± 0.04
contemporary	921.74 ± 362.59	1.86 ± 0.75	0.05 ± 0.01	1.1 ± 0.05

273 3.4. Canopy structure & FOTO texture analysis

274 Visual interpretation of the scenes provide evidence that most locations do not change dramatically
 275 with respect to canopy composition, except for the large areas of disturbances in contemporary fallow
 276 or young-regrowth plots. One marked difference is noted in the mono-dominant site 6 (Appendix
 277 Table 1). Here, the current mono-dominant *Brachystegia laurentii* is a recent development, changing the
 278 canopy structure visibly during the last half century (Figure 8). The previous varied canopy structure
 279 gave way to a more dense and uniform canopy. This is reflected in a change of the FOTO PC value from
 280 0.19 historically to its current value of 0.54. This historical value is similar to the mean of contemporary
 281 mono-dominant stands with PC averaging 0.34 ± 0.1 , and is only slightly higher than historical values
 282 for a mixed forest (0.18 ± 0.08). The reverse pattern is seen in the contemporary PC values. Here, the
 283 value of 0.54 exceeds those of most mono-dominant stands (0.35 ± 0.08), and is even further removed
 284 from the values noted for mixed forests (0.12 ± 0.03).

Using only small subsets around existing permanent sampling plots we show distinct differences between forest types, with PC values in both historical and contemporary imagery markedly higher for the mono-dominant forest types compared to all others (**Appendix Figure 4**). Provided that the young-regrowth and fallow permanent sampling plots have seen recent disturbance the Wilcoxon signed rank test on the mixed and mono-dominant plots between the historical and contemporary PC values did not show a significant difference ($p > 0.05$). Similarly, no significant different using PC values extracted from the whole scene analysis was noted ($p > 0.05$). Any relationships between contemporary Geo-Eye data and permanent sampling plot measurements of Above Ground Biomass, stem density and species richness were non-significant ($p > 0.05$, Appendix **Figures 5-7**).

Furthermore, visual inspection of the scene wide analysis suggests historical scenes do not show landscape wide canopy features (**Figure 9 A-B**), unlike the contemporary scene (**Figure 9 C-D**). Where the FOTO algorithm picks up landscape features such as changes in texture across the contemporary Geo-Eye scene (e.g. the river valley as a diagonal line in **Figure 9D**), however, no corresponding landscape patterns are found by the FOTO algorithm in the historical orthomosaic.

4. Discussion

Finely grained spatial data sources, such as remote sensing imagery, are rare before the satellite era (<1972). This lack of data limits our understanding of how forest structure has varied over longer time periods in remote areas. Long term assessment can be extended by using large inventories of historical aerial survey data [22,23,46]. Despite the difficulties in recovering this data and its limitations, such as invisible disturbances [47], remote sensing generally remains the best way to map and quantify LULCC [2]. In our study we used novel numerical remote sensing techniques to valorize, for the first time, historical remote sensing data in order to quantify (long term) land-use and land-cover change and canopy structural properties in the central Congo Basin. Despite these successes some methodological and research considerations remain.

4.1. Methodological considerations

4.1.1. Data recovery challenges

In our study the archive data recovered was limited to contact prints and therefore did not represent the true resolution of the original negative. In addition, analogue photography clearly produces a distinct softness compared to digital imagery (**Figure 8**). Despite favourable nadir image acquisitions [48] image softness combined with illumination effects between flight paths, and the self-similar nature of vast canopy expanses [49–51], limited our ability to provide wall-to-wall coverage of the entire dataset containing 334 images. Few man made features in the scenes also

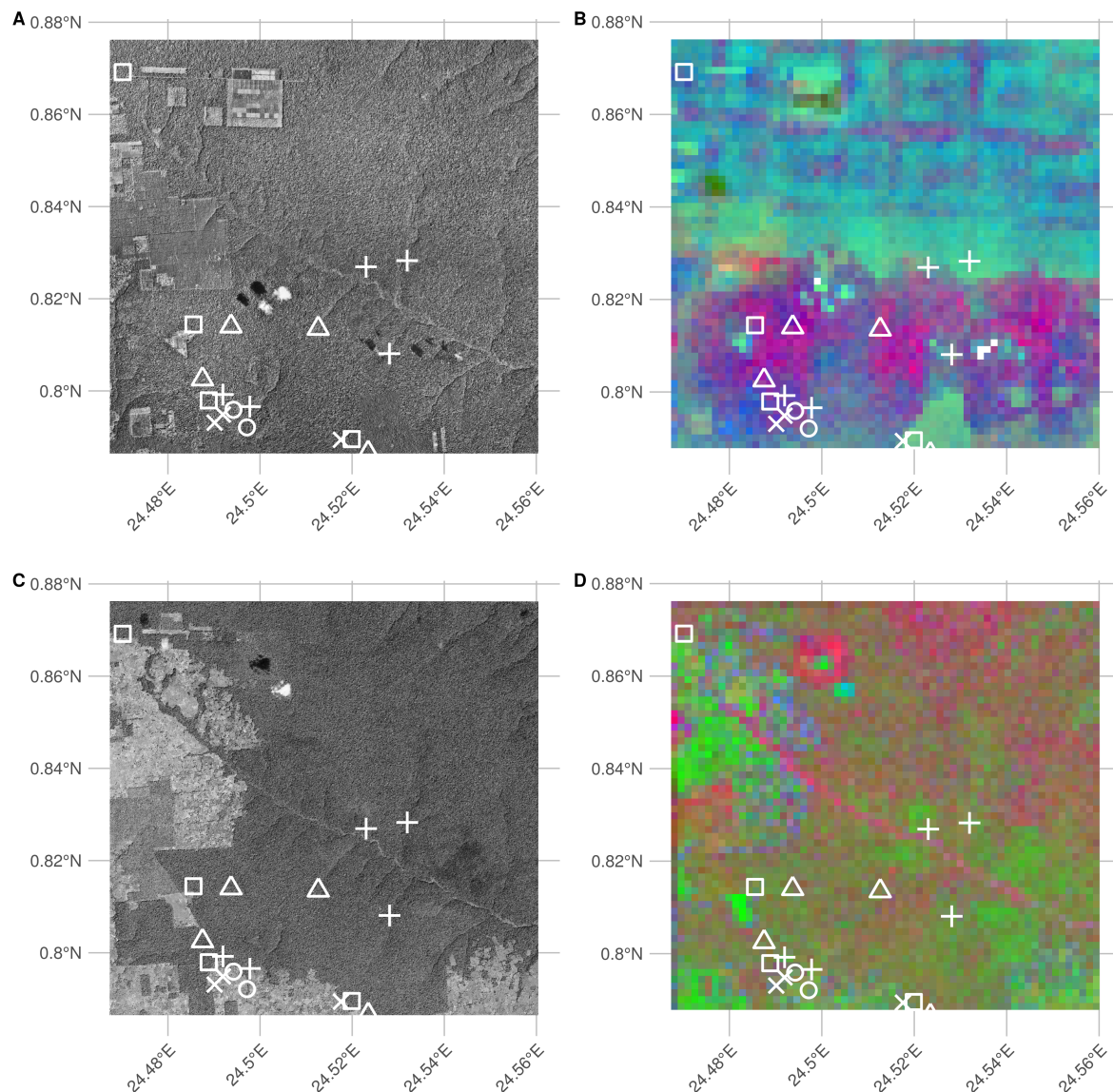


Figure 9. RGB visualizations of the first three principal components of scene wide FOTO texture analysis of historical and current (Geo-Eye) imagery. Current permanent sampling plots of mono-dominant, mixed, fallow and young (edge) forest plots are marked with open triangles, open circles, open squares and crosses, respectively.

made georeferencing challenging. Although the village of Yangambi provided a range of buildings as (hard-edge) references, other areas within the central Congo Basin might have fewer permanent structures and would require the use of soft-edged landscape features (e.g. trees, river outflows). Research has shown that soft-edged features can help georeference scenes even when containing few man-made features [52]. Our two step georeferencing approach resulted in a referencing accuracy of $\sim 4.7 \pm 4.3$ m across reference points. However, it shoud be noted that referencing accuracy of the final scene is less constrained toward the edges of the scene.

324 4.1.2. Land-use, Land-Cover change classification & validation

When classifying the orthomosaic into forest and non-forest states we favoured a deep learning supervised classification using a CNN over manual segmentation to guarantee an “apples-to-apples” comparison between the historical and the contemporary GFC forest cover map used in our analysis. We acknowledge that both the CNN and GFC land-use and land-cover maps use different underlying features, i.e. spatial or spectral data, yet attain a similarly high accuracy of up to 99% [1]. More so, when validating our CNN classifier against GFC data (Figure 7) for a contemporary high resolution Geo-Eye panchromatic image we reach an accuracy of $\sim 87\%$, despite a time difference of almost 60 years. Visual inspection of the classification data in Figure 7 suggests that the GFC map more often than not classifies non-forest areas as forest. Actual classification accuracy of our algorithm might therefore be higher than our reported value.

335 4.1.3. Scaling opportunities

Our approach uses broadly defined homogeneous polygons to construct a balanced dataset of synthetic landscapes. The methodology is analoguous to the use of sparse labelling as used by Buscombe and Ritchie [53] and contrasts with the standard methodologies which generally extract pixel (windows) [22] or delineate land cover classes [23] to drive a classifier or analysis. More so, the use of heavy image augmentation during model training sidesteps texture representation issues which affect classification of image scenes with inconsistent illumination or sharpness [25] or ad-hoc feature engineering [22]. The use of synthetic landscapes allowed us to account for most, but not all, of the variability within our orthomosaic. Our analysis has shown that despite being trained on historical data our model could map contemporary forest cover in remote sensing data with similar spatial and spectral characteristics (Figure 7), suggesting that the classifier consistently across works both space and time. We acknowledge that the use of synthetic landscapes is limited by the available homogeneous areas to sample from and the number of classes. Yet, the latter should not be a constraint as previous research efforts have focussed on simple forest loss maps [1].

350 4.2. Research context

351 4.3. Land-use, Land-Cover change & Above Ground Carbon

352 Our analysis shows that the majority of deforestation around Yangambi happened toward the late
353 1950's (~16200 ha). Considerable regrowth has occurred since the aerial survey was executed (~9918
354 ha), and socio-economic instability prevented further large scale forest exploitation. In particular, many
355 plantations have reached maturity and forest has re-established in previously cleared or disturbed
356 areas. The majority of this forest recovery takes the form of isolated patches of forest but is offset
357 by further deforestation of previously untouched forest. Generally, the function and structure of
358 forests can be influenced by forest edges that are located up to 1km away however most effects are
359 pronounced within the first 300m from the edge [54]. Our analysis of edge effects on AGC has shown
360 that the influence is negligible 200m away from the edge. Phillips *et al.* [55] have shown similar weak
361 responses to edge effects in the Amazon forest. Due to a lack of data on the extent (depth) of edge
362 effects and their influence on AGC beyond 200m we did not include any estimates of carbon loss
363 or gain within these zones. However, it must be stated that the influence of edges throughout the
364 landscape was not marginal. as these areas would account for 13151 ha. Thus edges could have a
365 substantial negative [10] or positive [56] influence on AGC. Similarly, uncertainties in how to explicitly
366 correct for plantations in the landscape present a further challenge. Thus although our estimates
367 are only indicative they do underscore the important influence of landscape structure when carbon
368 accounting. However, our findings do not indicate that deforestation in Congo basin is declining, on
369 the contrary.

370 Over the past half century there has been a clear shift in land use in Yangambi (Figure 5). Land
371 use has shifted away from for example a regular fishbone deforestation pattern that emerges when
372 (large scale) agricultural interests dominate the landscape [57], to a more fragmented landscape
373 (Figure 5D). The latter former? is consistent with historical land management at the time of the aerial
374 survey [44]. These regular patterns have since been reversed because of a decrease in large scale
375 intensive agriculture, replaced by ad-hoc small scale subsistence farming with large perimeter to area
376 relationships (i.e. ragged edges). Consequently, edge effects in the current landscape are far more
377 pronounced than in the historical scene.

378 Visual inspection of the images also suggests that reforestation within the historically cleared areas
379 and experimental plots is not necessarily limited to areas far removed from more densely populated
380 areas. For example, large reforested areas exist close to the Congo stream and Yangambi village itself
381 (Fig. 5). Here, regional political components, such as land leases and large scale ownership could
382 have played a role in safeguarding some of these areas for rewinding or sustainable management

[58,59]. Despite widespread anthropogenic influences throughout the tropics [32] the retention of these forested areas show the potential of explicit or implicit protective policy measures (e.g. INERA concessions, Bustillo *et al.* [44]) on a multi-decadal time scale. Forest regrowth in non-continuous areas within Yangambi could increase landscape connectivity and help increase biodiversity [9].

Our analysis therefore provides an opportunity to highlight and study those regions that have previously suffered confirmed long-term disturbances, and those that have been restored since. Assessments of old plantations and recovering clear-cut forests can serve as a guide to help estimate carbon storage capacity and forest recovery rates in managed and unmanaged conditions [18,20,60] over the mid- to long-term, in support of rewilding and general forest restoration [9,58,59]. In addition, mapping long-term edge effects can further support research into issues such as receding forest edges [54].

4.4. Canopy structure & FOTO texture analysis

Finally, the FOTO technique used to quantify relationships between canopy structure and forest characteristics rendered no valuable insights of either the historical orthomosaic or recent Geo-Eye scene. Similarly weak correlations were found previously by Solórzano *et al.* [61]. In contrast, site based texture metric statistics did show correspondence between historical and contemporary satellite imagery. None of them were either consistent or significant. Although visual interpretation shows distinctly different canopy structures (Figure 5) the differences in how resolution is defined and issues related to image quality prevented us from quantifying these further. Unlike large scale studies by Ploton *et al.* [14] we could not scale this technique to historical data. **The successful use of our CNN classification model on a contemporary remote sensing data does suggest that texture can be used to consistently capture canopy properties 60 years apart. This suggests inflexibilit on part of the FOTO technique in dealing with non-standardized data.** We advise that future valorisation efforts should preferentially work from foto negatives (if available) to ensure optimal data quality in resolution, contrast and sharpness.

5. Conclusion

Given the impact of tropical forest disturbances on atmospheric CO₂ emissions, biodiversity and ecosystem productivity accurate long term reporting on land-cover and land-use change in the pre-satellite era is an imperative. Our analysis of historical aerial survey images of the Central Congo Basin provides a window into the state of the forest at the start of the anthropocene. Efforts to quantify canopy texture and their link to carbon storage had limited to no success. We have shown that historical aerial survey data can be used to quantify land-use and land-cover change using a highly automated workflow to quantify the structure and extent of forest cover change that can help assess the

416 impact of fragmentation on above ground carbon stocks. We also show a shift from previously highly
417 structured industrial deforestation of large areas **for plantation purposes**, to discrete smallholder
418 clearing for farming, increasing landscape fragmentation but also opportunity for substantial regrowth.
419 Efforts to quantify canopy texture and their link to carbon storage had limited to no success. As such,
420 our analysis provides insights into the state of rarely studied tropical forests and the rate at which
421 deforestation and reforestation has taken place over a multi-decadal scale in the central Congo basin
422 providing a useful historical context to land-cover and land-use change spatial patterns for interpreting
423 past and ongoing field research in the area.

424 6. Additional Information and Declarations

425 6.1. Data availability

426 Hufkens et al. (2019). A curated dataset of aerial survey images over the central Congo Basin,
427 1958. Zenodo: doi.org/10.5281/zenodo.3547767. All data not included in the latter repository can be
428 found bundled with the analysis code as listed below. Proprietary datasets (i.e. Geo-Eye data) are not
429 shared, but purchase order numbers allow for acquisition of these datasets to ensure reproducibility.

430 6.2. Code availability

431 All analysis code is available as an R / python [62] projects (<https://khufkens.github.io/orthodrc>
432 & https://khufkens.github.io/orthodrc_cnn/). The analysis relied heavily on the ‘raster’ [63],
433 ‘RStoolbox’ [64], and ‘landscapemetrics’ [43] packages, while post-processing and plotting was
434 facilitated by the ‘tidyverse’ ecosystem [65], ‘ggthemes’ [66], ‘scales’ [67] and ‘cowplot’ [68]. Additional
435 plotting elements were formatted or provided by ‘sf’ [69] and ‘rnaturalearth’ [70] packages, respectively.
436 I’m grateful for the contributions to the scientific community by the developers of these packages.

437 **Acknowledgments:** This research was supported through the Belgian Science Policy office COBECORE
438 project (BELSPO; grant BR/175/A3/COBECORE). KH acknowledges funding from the European Union Marie
439 Skłodowska-Curie Action (project number 797668). I’m grateful for the support of Thales D’Haulleville
440 volunteering his time in scanning the images.

441 **Author Contributions:** K.H. conceived and designed the study, analyzed the data, prepared figures and tables,
442 authored, reviewed and approved the final draft of the manuscript. T.d.H. scanned all image data. E.K. and T.d.H.
443 provided plot based AGC estimates. T.D., K.J., E.K, H.B., P.S., F.V., S.M., M.A., J.V.D.B., H.V and L.W. reviewed the
444 final manuscript.

445 **Conflicts of Interest:** The authors declare no conflict of interest. The founding sponsors had no role in the design
446 of the study; in the collection, analyses, or interpretation of data; in the writing of the manuscript, and in the
447 decision to publish the results.

448 References

- 449 1. Hansen, M.C.; Potapov, P.V.; Moore, R.; Hancher, M.; Turubanova, S.A.; Tyukavina, A.; Thau, D.; Stehman,
450 S.V.; Goetz, S.J.; Loveland, T.R.; Kommareddy, A.; Egorov, A.; Chini, L.; Justice, C.O.; Townshend,
451 J.R.G. High-Resolution Global Maps of 21st-Century Forest Cover Change. *Science* **2013**, *342*, 850–853.
452 doi:10.1126/science.1244693.
- 453 2. Houghton, R.A.; House, J.I.; Pongratz, J.; van der Werf, G.R.; DeFries, R.S.; Hansen, M.C.; Le Quéré, C.;
454 Ramankutty, N. Carbon emissions from land use and land-cover change. *Biogeosciences* **2012**, *9*, 5125–5142.
455 doi:10.5194/bg-9-5125-2012.
- 456 3. Tyukavina, A.; Baccini, A.; Hansen, M.C.; Potapov, P.V.; Stehman, S.V.; Houghton, R.A.; Krylov, A.M.;
457 Turubanova, S.; Goetz, S.J. Aboveground carbon loss in natural and managed tropical forests from 2000 to
458 2012. *Environmental Research Letters* **2015**, *10*, 074002. doi:10.1088/1748-9326/10/7/074002.
- 459 4. van der Werf, G.R.; Morton, D.C.; DeFries, R.S.; Olivier, J.G.J.; Kasibhatla, P.S.; Jackson, R.B.; Collatz, G.J.;
460 Randerson, J.T. CO₂ emissions from forest loss. *Nature Geoscience* **2009**, *2*, 737–738. doi:10.1038/ngeo671.
- 461 5. Laurance, W.F.; Delamônica, P.; Laurance, S.G.; Vasconcelos, H.L.; Lovejoy, T.E. Rainforest fragmentation
462 kills big trees. *Nature* **2000**, *404*, 836–836. doi:10.1038/35009032.
- 463 6. Magnago, L.F.S.; Magrach, A.; Laurance, W.F.; Martins, S.V.; Meira-Neto, J.A.A.; Simonelli, M.; Edwards,
464 D.P. Would protecting tropical forest fragments provide carbon and biodiversity cobenefits under REDD+?
465 *Global Change Biology* **2015**, *21*, 3455–3468. doi:10.1111/gcb.12937.
- 466 7. Poorter, L.; Bongers, F. Leaf traits are good predictors of plant performance across 53 rain forest species.
467 *Ecology* **2006**, *87*, 1733–1743. doi:10.1890/0012-9658(2006)87[1733:LTAGPO]2.0.CO;2.
- 468 8. Barlow, J.; Lennox, G.D.; Ferreira, J.; Berenguer, E.; Lees, A.C.; Nally, R.M.; Thomson, J.R.; Ferraz, S.F.d.B.;
469 Louzada, J.; Oliveira, V.H.F.; Parry, L.; Ribeiro de Castro Solar, R.; Vieira, I.C.G.; Aragão, L.E.O.C.; Begotti,
470 R.A.; Braga, R.F.; Cardoso, T.M.; Jr, R.C.d.O.; Souza Jr, C.M.; Moura, N.G.; Nunes, S.S.; Siqueira, J.V.;
471 Pardini, R.; Silveira, J.M.; Vaz-de Mello, F.Z.; Veiga, R.C.S.; Venturieri, A.; Gardner, T.A. Anthropogenic
472 disturbance in tropical forests can double biodiversity loss from deforestation. *Nature* **2016**, *535*, 144–147.
473 doi:10.1038/nature18326.
- 474 9. Van de Perre, F.; Willig, M.R.; Presley, S.J.; Bapeamoni Andemwana, F.; Beeckman, H.; Boeckx, P.; Cooleman,
475 S.; de Haan, M.; De Kesel, A.; Dessein, S.; Grootaert, P.; Huygens, D.; Janssens, S.B.; Kearsley, E.; Kabeya,
476 P.M.; Leponce, M.; Van den Broeck, D.; Verbeeck, H.; Würsten, B.; Leirs, H.; Verheyen, E. Reconciling
477 biodiversity and carbon stock conservation in an Afrotropical forest landscape. *Science Advances* **2018**,
478 *4*, eaar6603. doi:10.1126/sciadv.aar6603.
- 479 10. Brinck, K.; Fischer, R.; Groeneveld, J.; Lehmann, S.; Dantas De Paula, M.; Pütz, S.; Sexton, J.O.; Song, D.;
480 Huth, A. High resolution analysis of tropical forest fragmentation and its impact on the global carbon
481 cycle. *Nature Communications* **2017**, *8*. doi:10.1038/ncomms14855.
- 482 11. Fauset, S.; Gloor, M.U.; Aidar, M.P.M.; Freitas, H.C.; Fyllas, N.M.; Marabesi, M.A.; Rochelle, A.L.C.;
483 Shenkin, A.; Vieira, S.A.; Joly, C.A. Tropical forest light regimes in a human-modified landscape. *Ecosphere*
484 **2017**, *8*, e02002. doi:10.1002/ecs2.2002.
- 485 12. Didham, R.K. Edge Structure Determines the Magnitude of Changes in Microclimate and Vegetation
486 Structure in Tropical Forest Fragments. *Biotropica* **1999**, *31*, 17–30.
- 487 13. Mitchard, E.T.A. The tropical forest carbon cycle and climate change. *Nature* **2018**, *559*, 527–534.
488 doi:10.1038/s41586-018-0300-2.
- 489 14. Ploton, P.; Pélassier, R.; Proisy, C.; Flavenot, T.; Barbier, N.; Rai, S.N.; Couturon, P. Assessing aboveground
490 tropical forest biomass using Google Earth canopy images. *Ecological Applications* **2012**, *22*, 993–1003.
- 491 15. Couturon, P.; Pelissier, R.; Nicolini, E.a.; Paget, D. Predicting tropical forest stand structure parameters
492 from Fourier transform of very high-resolution remotely sensed canopy images. *Journal of Applied Ecology*
493 **2005**, *42*, 1121–1128. doi:10.1111/j.1365-2664.2005.01097.x.
- 494 16. Barbier, N.; Couturon, P.; Proisy, C.; Malhi, Y.; Gastellu-Etchegorry, J.P. The variation of apparent crown
495 size and canopy heterogeneity across lowland Amazonian forests. *Global Ecology and Biogeography* **2010**,
496 *19*, 72–84. doi:10.1111/j.1466-8238.2009.00493.x.
- 497 17. DeFries, R.S.; Houghton, R.A.; Hansen, M.C.; Field, C.B.; Skole, D.; Townshend, J. Carbon emissions from
498 tropical deforestation and regrowth based on satellite observations for the 1980s and 1990s. *Proceedings of
499 the National Academy of Sciences* **2002**, *99*, 14256–14261. doi:10.1073/pnas.182560099.

- 500 18. Achard, F.; Beuchle, R.; Mayaux, P.; Stibig, H.J.; Bodart, C.; Brink, A.; Carboni, S.; Desclée, B.; Donnay, F.;
501 Eva, H.D.; Lüpi, A.; Rašić, R.; Seliger, R.; Simonetti, D. Determination of tropical deforestation rates and
502 related carbon losses from 1990 to 2010. *Global Change Biology* **2014**, *20*, 2540–2554. doi:10.1111/gcb.12605.
- 503 19. Ramankutty, N.; Foley, J.A. Estimating historical changes in global land cover: Croplands from 1700 to
504 1992. *Global Biogeochemical Cycles* **1999**, *13*, 997–1027. doi:10.1029/1999GB900046.
- 505 20. Sader, S.A.; Joyce, A.T. Deforestation Rates and Trends in Costa Rica, 1940 to 1983. *Biotropica* **1988**, *20*, 11.
506 doi:10.2307/2388421.
- 507 21. Willcock, S.; Phillips, O.L.; Platts, P.J.; Swetnam, R.D.; Balmford, A.; Burgess, N.D.; Ahrends, A.; Bayliss,
508 J.; Doggart, N.; Doody, K.; Fanning, E.; Green, J.M.H.; Hall, J.; Howell, K.L.; Lovett, J.C.; Marchant, R.;
509 Marshall, A.R.; Mbilinyi, B.; Munishi, P.K.T.; Owen, N.; Topp-Jorgensen, E.J.; Lewis, S.L. Land cover
510 change and carbon emissions over 100 years in an African biodiversity hotspot. *Global Change Biology* **2016**,
511 *22*, 2787–2800. doi:10.1111/gcb.13218.
- 512 22. Song, D.X.; Huang, C.; Sexton, J.O.; Channan, S.; Feng, M.; Townshend, J.R. Use of Landsat and
513 Corona data for mapping forest cover change from the mid-1960s to 2000s: Case studies from the Eastern
514 United States and Central Brazil. *ISPRS Journal of Photogrammetry and Remote Sensing* **2015**, *103*, 81–92.
515 doi:10.1016/j.isprsjprs.2014.09.005.
- 516 23. Nita, M.D.; Munteanu, C.; Gutman, G.; Abrudan, I.V.; Radloff, V.C. Widespread forest cutting in the
517 aftermath of World War II captured by broad-scale historical Corona spy satellite photography. *Remote
518 Sensing of Environment* **2018**, *204*, 322–332. doi:10.1016/j.rse.2017.10.021.
- 519 24. Buitenhof, R.; Bond, W.J.; Stevens, N.; Trollope, W.S.W. Increased tree densities in South African
520 savannas: >50 years of data suggests CO₂ as a driver. *Global Change Biology* **2012**, *18*, 675–684.
521 doi:10.1111/j.1365-2486.2011.02561.x.
- 522 25. Hudak, A.T.; Wessman, C.A. Textural Analysis of Historical Aerial Photography to Characterize Woody
523 Plant Encroachment in South African Savanna. *Remote Sensing of Environment* **1998**, *66*, 317–330.
524 doi:10.1016/S0034-4257(98)00078-9.
- 525 26. Okeke, F.; Karnieli, A. Methods for fuzzy classification and accuracy assessment of historical aerial
526 photographs for vegetation change analyses. Part I: Algorithm development. *International Journal of Remote
527 Sensing* **2006**, *27*, 153–176. doi:10.1080/01431160500166540.
- 528 27. Frankl, A.; Seghers, V.; Stal, C.; De Maeyer, P.; Petrie, G.; Nyssen, J. Using image-based modelling
529 (SfM-MVS) to produce a 1935 ortho-mosaic of the Ethiopian highlands. *International Journal of Digital Earth*
530 **2015**, *8*, 421–430. doi:10.1080/17538947.2014.942715.
- 531 28. Nyssen, J.; Petrie, G.; Mohamed, S.; Gebremeskel, G.; Seghers, V.; Debever, M.; Hadgu, K.M.; Stal, C.; Billi,
532 P.; Demaeyer, P.; Haile, M.; Frankl, A. Recovery of the aerial photographs of Ethiopia in the 1930s. *Journal
533 of Cultural Heritage* **2016**, *17*, 170–178. doi:10.1016/j.culher.2015.07.010.
- 534 29. Lewis, S.L.; Lopez-Gonzalez, G.; Sonké, B.; Affum-Baffoe, K.; Baker, T.R.; Ojo, L.O.; Phillips, O.L.; Reitsma,
535 J.M.; White, L.; Comiskey, J.A.; Djuiokou, K.M.N.; Ewango, C.E.N.; Feldpausch, T.R.; Hamilton, A.C.;
536 Gloor, M.; Hart, T.; Hladik, A.; Lloyd, J.; Lovett, J.C.; Makana, J.R.; Malhi, Y.; Mbago, F.M.; Ndangalasi,
537 H.J.; Peacock, J.; Peh, K.S.H.; Sheil, D.; Sunderland, T.; Swaine, M.D.; Taplin, J.; Taylor, D.; Thomas, S.C.;
538 Votere, R.; Wöll, H. Increasing carbon storage in intact African tropical forests. *Nature* **2009**, *457*, 1003–1006.
539 Publisher: Earth and Biosphere Institute, School of Geography, University of Leeds, Leeds LS2 9JT, UK.
540 s.l.lewis@leeds.ac.uk.
- 541 30. Butsic, V.; Baumann, M.; Shortland, A.; Walker, S.; Kuemmerle, T. Conservation and conflict in the
542 Democratic Republic of Congo: The impacts of warfare, mining, and protected areas on deforestation.
543 *Biological Conservation* **2015**, *191*, 266–273. doi:10.1016/j.biocon.2015.06.037.
- 544 31. Kearsley, E.; de Haulleville, T.; Hufkens, K.; Kidimbu, A.; Toirambe, B.; Baert, G.; Huygens, D.; Kebede,
545 Y.; Defourny, P.; Bogaert, J.; Beeckman, H.; Steppe, K.; Boeckx, P.; Verbeeck, H. Conventional tree
546 height-diameter relationships significantly overestimate aboveground carbon stocks in the Central Congo
547 Basin. *Nature communications* **2013**, *4*, 2269. doi:10.1038/ncomms3269.
- 548 32. Lewis, S.L.; Maslin, M.A. Defining the Anthropocene. *Nature* **2015**, *519*, 171–180. doi:10.1038/nature14258.
- 549 33. Bauters, M.; Ampoorter, E.; Huygens, D.; Kearsley, E.; De Haulleville, T.; Sellan, G.; Verbeeck, H.; Boeckx,
550 P.; Verheyen, K. Functional identity explains carbon sequestration in a 77-year-old experimental tropical
551 plantation. *Ecosphere* **2015**, *6*, art198. doi:10.1890/ES15-00342.1.

- 552 34. Zuiderveld, K. Contrast Limited Adaptive Histogram Equalization. In *Graphics GEMs IV*; Academic Press:
553 San Diego, CA, USA, 1994; pp. 474–485.
- 554 35. Ullman, S. The Interpretation of Structure from Motion. *Proceedings of the Royal Society of London. Series B, Biological Sciences* **1979**, *203*, 405–426.
- 556 36. QGIS Development team., QGIS Geographic Information System., 2018. Available at: <http://qgis.osgeo.org>.
- 557 37. Ronneberger, O.; Fischer, P.; Brox, T. U-Net: Convolutional Networks for Biomedical Image Segmentation.
558 In *Medical Image Computing and Computer-Assisted Intervention – MICCAI 2015*; Navab, N.; Hornegger, J.;
559 Wells, W.M.; Frangi, A.F., Eds.; Springer International Publishing: Cham, 2015; Vol. 9351, pp. 234–241.
560 doi:10.1007/978-3-319-24574-4_28.
- 562 38. Chollet, F. Keras, 2015. Available at: <https://github.com/fchollet/keras>.
- 563 39. Yakubovskiy, P. Segmentation Models, 2019. Available at: https://github.com/qubvel/segmentation_models.
- 565 40. Martín Abadi.; Ashish Agarwal.; Paul Barham.; Eugene Brevdo.; Zhifeng Chen.; Craig Citro.; Greg S.
566 Corrado.; Andy Davis.; Jeffrey Dean.; Matthieu Devin.; Sanjay Ghemawat.; Ian Goodfellow.; Andrew
567 Harp.; Geoffrey Irving.; Michael Isard.; Jia, Y.; Rafal Jozefowicz.; Lukasz Kaiser.; Manjunath Kudlur.; Josh
568 Levenberg.; Dandelion Mané.; Rajat Monga.; Sherry Moore.; Derek Murray.; Chris Olah.; Mike Schuster.;
569 Jonathon Shlens.; Benoit Steiner.; Ilya Sutskever.; Kunal Talwar.; Paul Tucker.; Vincent Vanhoucke.; Vijay
570 Vasudevan.; Fernanda Viégas.; Oriol Vinyals.; Pete Warden.; Martin Wattenberg.; Martin Wicke.; Yuan Yu.;
571 Xiaoqiang Zheng. TensorFlow: Large-Scale Machine Learning on Heterogeneous Systems, 2015. Available
572 at: <https://www.tensorflow.org/>.
- 573 41. Kingma, D.P.; Ba, J. Adam: A Method for Stochastic Optimization. *arXiv:1412.6980 [cs]* **2017**. arXiv:
574 1412.6980.
- 575 42. Dale, M.R.T. *Spatial pattern analysis in plant ecology*; Cambridge studies in ecology, Cambridge University
576 Press: Cambridge ; New York, 1999.
- 577 43. Hesselbarth, M.H.K.; Sciaiani, M.; With, K.A.; Wiegand, K.; Nowosad, J. landscapemetrics: an open-source
578 R tool to calculate landscape metrics. *Ecography* **2019**.
- 579 44. Bustillo, E.; Raets, L.; Beeckman, H.; Bourland, N.; Rousseau, M.; Hubau, W.; De Mil, T. Evaluation du
580 potentiel énergétique de la biomasse aérienne ligneuse des anciennes plantations de l'INERA Yangambi.
581 Technical report, CIFOR, 2018.
- 582 45. Couteron, P. Quantifying change in patterned semi-arid vegetation by Fourier analysis of digitized aerial
583 photographs. *International Journal of Remote Sensing* **2002**, *23*, 3407–3425. doi:10.1080/01431160110107699.
- 584 46. Kadmon, R.; Harari-Kremer, R. Studying Long-Term Vegetation Dynamics Using Digital
585 Processing of Historical Aerial Photographs. *Remote Sensing of Environment* **1999**, *68*, 164–176.
586 doi:10.1016/S0034-4257(98)00109-6.
- 587 47. Peres, C.A.; Barlow, J.; Laurance, W.F. Detecting anthropogenic disturbance in tropical forests. *Trends in
588 Ecology & Evolution* **2006**, *21*, 227–229. doi:10.1016/j.tree.2006.03.007.
- 589 48. Verhoeven, G. BRDF and its Impact on Aerial Archaeological Photography: BRDF and its impact on aerial
590 archaeological photography. *Archaeological Prospection* **2017**, *24*, 133–140. doi:10.1002/arp.1559.
- 591 49. Park, J.Y.; Muller-Landau, H.C.; Lichstein, J.W.; Rifai, S.W.; Dandois, J.P.; Bohlman, S.A. Quantifying Leaf
592 Phenology of Individual Trees and Species in a Tropical Forest Using Unmanned Aerial Vehicle (UAV)
593 Images. *Remote Sensing* **2019**, *11*, 1534. doi:10.3390/rs11131534.
- 594 50. Simini, F.; Anfodillo, T.; Carrer, M.; Banavar, J.R.; Maritan, A. Self-similarity and scaling
595 in forest communities. *Proceedings of the National Academy of Sciences* **2010**, *107*, 7658–7662.
596 doi:10.1073/pnas.1000137107.
- 597 51. Sole, R.V.; Manrubia, S.C. Self-similarity in rain forests: evidence for a critical state. *Physical Review E* **1995**,
598 *51*, 6250 – 6253.
- 599 52. Hughes, M.L.; McDowell, P.F.; Marcus, W.A. Accuracy assessment of georectified aerial photographs:
600 Implications for measuring lateral channel movement in a GIS. *Geomorphology* **2006**, *74*, 1–16.
601 doi:10.1016/j.geomorph.2005.07.001.
- 602 53. Buscombe, D.; Ritchie, A. Landscape Classification with Deep Neural Networks. *Geosciences* **2018**, *8*, 244.
603 doi:10.3390/geosciences8070244.

- 604 54. Gascon, C.; Williamson, G.B.; Fonseca, G.A.B.d. Receding Forest Edges and Vanishing Reserves. *Science, New Series* **2000**, *288*, 1356–1358.
- 605 55. Phillips, O.L.; Rose, S.; Mendoza, A.M.; Vargas, P.N. Resilience of Southwestern Amazon Forests to Anthropogenic Edge Effects. *Conservation Biology* **2006**, *20*, 1698–1710. doi:10.1111/j.1523-1739.2006.00523.x.
- 606 56. Reinmann, A.B.; Hutyra, L.R. Edge effects enhance carbon uptake and its vulnerability to climate change in temperate broadleaf forests. *Proceedings of the National Academy of Sciences* **2017**, *114*, 107–112. doi:10.1073/pnas.1612369114.
- 607 57. Arima, E.Y.; Walker, R.T.; Perz, S.; Souza, C. Explaining the fragmentation in the Brazilian Amazonian forest. *Journal of Land Use Science* **2015**, pp. 1–21. doi:10.1080/1747423X.2015.1027797.
- 608 58. Arima, E.Y.; Barreto, P.; Araújo, E.; Soares-Filho, B. Public policies can reduce tropical deforestation: Lessons and challenges from Brazil. *Land Use Policy* **2014**, *41*, 465–473. doi:10.1016/j.landusepol.2014.06.026.
- 609 59. Larson, A.M. Forest tenure reform in the age of climate change: Lessons for REDD+. *Global Environmental Change* **2011**, *21*, 540–549. doi:10.1016/j.gloenvcha.2010.11.008.
- 610 60. Gourlet-Fleury, S.; Mortier, F.; Fayolle, A.; Baya, F.; Ouédraogo, D.; Bénédict, F.; Picard, N. Tropical forest recovery from logging: a 24 year silvicultural experiment from Central Africa. *Philosophical Transactions of the Royal Society B: Biological Sciences* **2013**, *368*, 20120302. doi:10.1098/rstb.2012.0302.
- 611 61. Solórzano, J.V.; Gallardo-cruz, J.A.; González, E.J.; Peralta-carreta, C.; Hernández-gómez, M.; Oca, A.F.m.D.; Cervantes-jiménez, L.G.; Solórzano, J.V.; Gallardo-cruz, J.A.; González, E.J.; Peralta-carreta, C.; Hernández-gómez, M.; Oca, A.F.m.D.; Cervantes-jiménez, L.G. Contrasting the potential of Fourier transformed ordination and gray level co-occurrence matrix textures to model a tropical swamp forest 's structural and diversity attributes. *Journal of Applied Remote Sensing* **2018**, *12*, 036006. doi:10.1111/1.JRS.12.036006.
- 612 62. R Core Team. *R: A Language and Environment for Statistical Computing*; R Foundation for Statistical Computing: Vienna, Austria, 2019.
- 613 63. Hijmans, R.J. raster: Geographic Data Analysis and Modeling, 2019. Available at: <https://CRAN.R-project.org/package=raster>.
- 614 64. Leutner, B.; Horning, N.; Schwalb-Willmann, J. RStoolbox: Tools for Remote Sensing Data Analysis, 2019. Available at: <https://CRAN.R-project.org/package=RStoolbox>.
- 615 65. Wickham, H. tidyverse: Easily Install and Load the 'Tidyverse', 2017. Available at: <https://CRAN.R-project.org/package=tidyverse>.
- 616 66. Arnold, J.B. ggthemes: Extra Themes, Scales and Geoms for 'ggplot2', 2019. Available at: <https://CRAN.R-project.org/package=ggthemes>.
- 617 67. Wickham, H. scales: Scale Functions for Visualization, 2018. Available at: <https://CRAN.R-project.org/package=scales>.
- 618 68. Wilke, C.O. cowplot: Streamlined Plot Theme and Plot Annotations for 'ggplot2', 2019. Available at: <https://CRAN.R-project.org/package=cowplot>.
- 619 69. Pebesma, E. Simple Features for R: Standardized Support for Spatial Vector Data. *The R Journal* **2018**, *10*, 439–446. doi:10.32614/RJ-2018-009.
- 620 70. South, A. rnaturalearth: World Map Data from Natural Earth, 2017. Available at: <https://CRAN.R-project.org/package=rnaturalearth>.